Single-nanoparticle-thick three-phase plasmonic catalysis for efficient nitrogen photofixation without sacrificial agents

Siew Kheng Boong[a], Carice Chong[a], Jiajia Zhang[a], Tharishinny Raja Mogan[a], Yimeng Ni[a], Haitao Li[b], Hiang Kwee Lee[a,c,d*]

Affiliations:

[a] Division of Chemistry and Biological Chemistry, School of Chemistry, Chemical Engineering and Biotechnology, Nanyang Technological University, 21 Nanyang Link, Singapore 637371, Singapore.

[b] School of Chemistry and Chemical Engineering, Yangzhou University, Yangzhou, 225002, PR China.

[c] Institute of Materials Research and Engineering, The Agency for Science, Technology and Research (A∗STAR), 2 Fusionopolis Way, #08-03, Innovis, 138634, Singapore.

[d] Centre for Hydrogen Innovations, National University of Singapore, E8, 1 Engineering drive 3, 117580, Singapore.

* Corresponding author:

E-mail address: hiangkwee@ntu.edu.sg (Hiang Kwee Lee)

Abstract

Plasmonic catalysis promises efficient green ammonia production from nitrogen gas, water, and (sun)light. However, existing designs are limited by poor catalytic performance and reliance on organic sacrificial agents. Here, we achieve efficient ammonia photosynthesis at ambient conditions without sacrificial agent by introducing a single-particle-thick plasmonic superlattice at a three-phase catalytic interface. By organizing Ag-square superlattice on a hydrogel to create an electromagnetically hot solid-liquid-gas tri-interface, our three-phase plasmonic catalyst achieves a superior ammonia formation rate of 101 μmol h^{-1} g^{-1}, surpassing conventional two-phase configuration by ~33-fold. More importantly, our unique design attains up to ~26-fold and ~2500-fold enhancements in ammonia formation rate and apparent quantum yield, respectively. Mechanistic investigations uncover the importance of three-phase plasmonic interface to efficiently concentrate light and enrich immiscible gas-liquid reactants at point-of-catalysis, thereby boosting nitrogen photofixation. Our work offers valuable insights for designing multifunctional plasmonic ensembles towards sustainable chemical manufacturing and a carbon-free hydrogen economy.

Keywords: Three-phase interface, plasmon catalysis, nitrogen fixation, electromagnetic hotspot, light-concentrating

1. Introduction

Plasmonic catalysis promises efficient production of green ammonia from naturally abundant nitrogen gas, water, and (sun)light, offering huge potential to address sustainability challenges in the energy, chemical, and agricultural industries.[1-5] Unlike semiconductor photocatalysis, plasmonic catalysis utilizes metal nanoparticles to focus light energy directly on catalytic sites via unique localized surface plasmon resonances (LSPRs).[6-9] The subsequent non-radiative decay of the enhanced electromagnetic field generates hot carriers (e.g., hot electrons and hot holes), enabling facile reaction activation even at ambient conditions.[10,11] This approach is thus attractive for circumventing longstanding limitations associated with the traditional Haber-Bosch process, such as the requirement for extreme reaction conditions (e.g. 773 K and 200 atm), high energy demand, and a large carbon footprint.[12-15]

Current plasmonic catalysis designs typically rely on semiconductor/metal co-catalysts to form heterojunctions for enhancing photocarrier separation and utilization during chemical reactions.[16-24] For instance, the $Au/SrTiO_3/Ru$ ensemble has demonstrated improved charge separations, facilitating nitrogen reduction into ammonia at a rate of 1.87×10^{-8} g h^{-1} cm^{-2} using ethanol as a hole scavenger.[25] More recently, we introduced a unique approach to enhance plasmonic catalysis without requiring a co-catalyst. We achieved this by creating an electromagnetically hot plasmonic catalyst through the formation of a plasmonic superlattice, resulting in a relatively high ammonia formation rate of 55.3 μmol h^{-1} g^{-1} using 1-propanol as a sacrificial agent.[26] However, these reported designs face challenges in catalytic performance due to the difficulty of effectively delivering nitrogen (N_2) gas reactant to the plasmonic catalyst. This issue arises from the poor solubility of nitrogen gas in most liquids and its slow diffusivity.[27,28] Another major limitation is the reliance on fossil-derived organic molecules (e.g., alcohols, lactic acid) as photo-hole scavengers in many photocatalytic approaches to complete the photocatalytic cycle.[17,25,29] This drawback is attributed to the sluggish four-electrons oxygen evolution reaction of water and the potential formation of micro/nanobubbles that could deactivate catalytic sites.[30]

Notably, three-phase catalysis holds immense potential in alleviating mass transportation bottleneck to further enhance plasmonic catalysis.[31] Three-phase catalytic platforms generally entail forming a tri-interface among solid nanocatalysts, the liquid medium, and the gas reactant.[32,33] Common designs involve depositing hydrophilic nanocatalysts onto hydrophobic porous supports and subsequently bringing them in contact with water to create the three-phase interface.[34-36] This approach provides two key advantages. (1) Enhanced interactions between gas and liquid phase reactants, as gas reactants do not have to be soluble in liquid reaction medium. (2) The prevention of bubble nucleation on catalyst surfaces by facilitating the transfer of gaseous products into the continuous gas phase upon their formation.[37-39] However, the lack of control over catalyst deposition (e.g., thickness, distribution, shape) on hydrophobic support impedes the precise design of the three-phase interface. This limitation severely reduces catalytic efficiency and catalyst utilization because a large portion of the catalyst may become immersed in liquid, rendering it ineffective for three-phase catalysis.

Herein, we achieve efficient green ammonia photosynthesis without a sacrificial agent by introducing an effective three-phase plasmonic catalytic design. This design is realized through the self-assembly of anisotropic plasmonic nanocatalysts into an ordered particle monolayer directly at the liquid-air interface. Our strategy integrates two crucial concepts. (1) The formation of a single-particle-thick plasmonic superlattice at the point-of-reaction to create large-area, intense plasmonic hotspots for driving nitrogen-to-ammonia transformations while maximizing the utilization of catalytic material. (2) This two-dimensional superlattice also creates abundant three-phase catalytic sites consisting of the plasmonic nanoparticles (solid phase), hydrogel (liquid phase), and a continuous N_2 environment (gas phase). Notably, the use of hydrogel as a liquid phase is unprecedented in three-phase catalysis and plays a pivotal role in maintaining the superlattice structural configuration while providing a constant aqueous reaction medium for nitrogen reduction. Our unique design thus aims to overcome the performance bottleneck in light-driven nitrogen reduction reactions by concurrently mitigating ineffective gas transportation and weak field enhancement present in most traditional two-phase plasmonic catalysis.

We first demonstrate the formation of an electromagnetically hot square-based plasmonic superlattice on a hydrogel surface using silver (Ag) nano-octahedra as a building block due to its strong field confinement at tips and edges from the lightning-rod effect. More importantly, our three-phase plasmonic catalyst achieves efficient ammonia formation at 101 μmol h^{-1} g^{-1}, even without the use of any chemical additive as a sacrificial agent. This superior performance surpasses traditional two-phase catalysis by ~33-fold and demonstrates up to ~26-fold and ~2500-fold enhancements in ammonia formation rate and apparent quantum yield, respectively, compared to other emerging photocatalytic platforms utilizing co-catalysts and organic hole scavengers. Comprehensive mechanistic studies underscore the critical role of the three-phase plasmonic interface in simultaneously enriching immiscible liquid-gas reactants and concentrating light on catalytic surfaces for driving ammonia photosynthesis using plasmons. By enabling the effective manipulation of molecules and light at the nanoscale, our study provides valuable insights for designing the next generation of plasmonic ensembles to realize high-performance and truly green ammonia production.

2. Experimental

2.1 Chemicals

Silver nitrate (≥ 99%), anhydrous 1,5-pentanediol (PD, ≥ 97%), poly(vinylpyrrolidone) (PVP, average MW = 55000), copper(II) chloride ($CuCl_2$, 97%), 4-methylbenzenethiol (4-MBT, 98%), 1-dodecanethiol ($C_{12}SH$, ≥ 98%), ammonium sulfate (≥ 99.0%), sodium nitroprusside dihydrate (≥ 99%, ACS reagent; Reag. Ph. Eur), sodium dichloroisocyanurate dihydrate (≥ 98.0%), phenol (≥ 99%, purified by redistillation), decane (≥ 95%), methylene blue, and bromophenol blue (ACS reagent) were purchased from Sigma-Aldrich; Sodium hydroxide (AR grade) was from Schedelco; Sodium sulfate (anhydrous, AR grade) was from UNI-Chem; Ammonium chloride (AR grade) was from Quality Reagent Chemical; KELCOGEL® gellan gum was from CP Kelco; SYLGARD™ 184 silicone elastomer kit (base and curing agent) was from Dow; Sulfuric acid (H_2SO_4, 95-97%) and hydrochloric acid (HCl, 37%) were from Honeywell; Ethanol (EtOH, ≥ 98%, AR grade), acetone (≥ 99.8%, AR grade), and propan-2-ol (IPA, ≥ 99.5%) was obtained from Fisher Scientific; Nitrogen (N_2, ALPHAGAZ 1; 99.999%) and argon (Ar, 99.9995%) were purchased from Leeden National Oxygen Ltd. All chemicals were used without further purification. Milli-Q water (> 18.0 MΩ.cm) was purified with a Sartorius Arium 611 ® UV ultrapure water system.

2.2 Synthesis and purification of silver octahedra

The preparation of Ag octahedra was carried out following the polyol reduction method reported in the literature.[40] Ag nanocube was first synthesized and used as seeds for the subsequent growth into Ag octahedra. Briefly, 10 mL of copper (II) chloride (8 mg/mL), poly(vinylpyrrolidone) (20 mg/mL), and silver nitrate (20 mg/mL) were separately dissolved in 1,5-pentanediol (PD). 35 μL copper (II) chloride solution was then added to the silver nitrate precursor. Then, a round-bottomed flask containing 20 mL 1,5-pentanediol was heated to 190 ^oC for 10 min. 250 μL poly(vinylpyrrolidone) precursor was added to flask dropwise every 30 s, while 500 μL silver nitrate precursor was added in one shot every minute. The process was allowed to continue for ~16 min to obtain Ag nanocubes. To synthesize the Ag octahedra, the as-synthesized Ag nanocubes were subjected to the same injection procedure using 30 mL of poly(vinylpyrrolidone) precursor (20 mg/mL) and silver nitrate solution (40 mg/mL, also contained 120 μL $CuCl_2$).

For the purification of Ag octahedra, the final solution was centrifuged to remove 1,5-pentanediol with acetone and ethanol. The Ag octahedra solution was then dispersed in 20 mL ethanol and 100 mL aqueous poly(vinylpyrrolidone) solution (0.2 g/L). The resulting solution was vacuum filtered through Durapore® polyvinylidene fluoride filter membranes (Millipore) with pore sizes of 5000 nm and 650 nm, repeated at least 2 times for each pore size. The Ag octahedra was redispersed in ethanol to make up a concentration of ~10 mg/mL. SEM imaging was performed and the edge lengths of Ag

octahedra were measured using ImageJ software.

2.3 Surface modifications of Ag octahedra

Ag octahedra solution (300 μL, 10 mg/mL) was dispersed in a mixture of 450 μL of ethanol (EtOH) and 750 μL of propan-2-ol (IPA). 150 μL of 10 mM 1-dodecanethiol solution (in ethanol) was then added dropwise to this dispersion under stirring. Ligand exchange was allowed to take place for 2 h, washed with copious amount of solvent (EtOH and IPA), and subsequently redispersed in 1.5 ml of EtOH/IPA (1:1). A fresh ethanolic solution of 1-dodecanethiol (150 μL) was then added to the Ag octahedra dispersion under stirring for another 2 h. Finally, the Ag octahedra was washed with copious amount of IPA/H_2O (1:1) solution and re-dispersed in 750 μL of IPA/H_2O (1:1) for subsequent use.

2.4 Interfacial self-assembly and gel-trapping of Ag octahedra at water-decane interface

The gel-trapping experiment was carried out following the method described in literature.[40] Aqueous gellan gum solution (GG; 2 mL, 2 wt%) was used as the water phase and decane was used as the oil phase to create a liquid-liquid interface. The gellan gum solution was first heated to ~80 °C in an oil bath to ensure that the gel was fully hydrated, and the hydrogel solution was subjected to vacuum for several times to remove air bubbles trapped within the solution. Subsequently, pre-heated decane was added on top of the gellan gum solution. Ag octahedra (~300 μL) in IPA/H_2O (1:1) solution was then added onto the water-oil interface and the entire mixture was left at 80 °C for ~10 min before allowing it to slowly cool to room temperature. Once the gel had set in the aqueous phase, the oil phase was then decanted gently. The substrates were kept in fridge before use.

2.5 Preparation of Ag superlattice/PDMS

A thin layer of premixed polydimethylsiloxane (PDMS) precursor mixture (5:1; elastomer base: curing agent) was poured over the Ag superlattice on gellan gum and left to cure at ~30 ^oC in the oven for overnight. The curing of the PDMS layer enabled the transfer of the assembled Ag array onto the hardened PDMS support for subsequent characterization of the optical properties and used as control experiments in plasmonic catalysis.

2.6 Acid treatment of plasmonic Ag-square superlattice prior to nitrogen reduction reaction

Ag-square superlattices on gellan gum (1.5 × 1.5 × 0.5 cm) were immersed in 12.5mL of 1M HCl in 1:1 EtOH:H_2O solution for 30 min to remove the surface thiols that were previously used to guide the self-assembly process. The platforms were then washed with ample 1:1 EtOH:H_2O solution. Next, the excess acid was removed by immersing the substrates in 30 mL H_2O with slow stirring for 10 min. This acid removal process was repeated for four rounds using fresh H_2O during each cycle. The Ag-

square superlattice surface was blown dried using N_2 gas stream and stored in fridge for subsequent experiments.

2.7 Preparation of PVP- or $C_{12}SH$-capped Ag film for XPS characterization

Ag films were deposited using a thermal evaporator deposition system from Syskey Technology Corporation (Taiwan). A 25 nm Ag was deposited on an O_2 plasma-treated Si wafer (1 cm × 1 cm) at a deposition rate of 0.8 Å/s. The deposited rate was monitored in situ through a quartz crystal microbalance. Ag source with 99.99% purity was purchased from Zhongnuo Advanced Material (Beijing) Technology co., Ltd. The Ag films were subsequently functionalized via immersion in ethanolic PVP or $C_{12}SH$ solutions (2.5 mL, 10 mM) for overnight. The PVP- and $C_{12}SH$-grafted Ag films were then washed with ample amount of ethanol and blown dried using N_2 gas stream. Similarly, the PVP- and $C_{12}SH$-grafted Ag films were treated with 1M HCl in 1:1 EtOH:H_2O solution for 30 min, washed with copious amount of 1:1 EtOH:H_2O solution to remove excess acid, and subsequently dried using nitrogen gas stream to give the acid treated platforms. Notably, the PVP- and $C_{12}SH$-grafted Ag films were used to mimic the Ag-square superlattice owing to their larger Ag surface area necessary for XPS characterizations.

2.8 Preparation of disorganized Ag octahedra for SERS and contact angle measurements

A same amount of ethanolic PVP-capped Ag octahedra was drop-casted on Si wafer (area, 2.25 cm^2) to prepare a disorganized Ag array for comparison. The Si wafer was surface treated with oxygen plasma before drop-casting of the Ag octahedra.

2.9 SERS measurements of Ag superlattice/GG and drop-casted Ag octahedra

The platforms were functionalized with 4-methylbenzenethiol (4-MBT) by immersed in ethanolic 4-MBT solutions (5 mL, 10 mM) for overnight. 4-MBT-grafted Ag substrates were then washed with copious amount of ethanol and blown dried using N_2 gas stream. A 2M ethanolic solution of 4-MBT was used to record the normal Raman spectrum.

2.10 Photocurrent measurements

The acid-treated Ag-square superlattice on PDMS was coated with 10 nm of Pt layer using JEOL JFC-1600 Auto Fine Coater to improve electrical conductivity for photocurrent measurements. The photoelectrochemical setup included an argon-saturated aqueous Na_2SO_4 electrolyte solution (0.5 M), a Ag-square superlattice (area, 2.25 cm^2; working electrode), a Pt wire (counter electrode), and Ag/AgCl (3M KCl; reference electrode). A potential of -2.5V (vs. Ag/AgCl; Figure 1E) was applied under a 100W LED white light irradiation (400 – 750 nm, 277mW/cm^2) to measure photocurrent response and the data was acquired with an interval of 0.01 s.

2.11 Evaluation on gas access to target interface in three-phase and two-phase setups

The pure gellan gum (dimension, 1.5 × 0.75 × 0.5 cm) was loaded with basified bromophenol blue dye (pH 9) before the reaction. The dye-containing gellan gum was placed in a vial while being directly exposed to a gas phase or immersed in water. N_2 gas (20 sccm) was subsequently purged into concentrated hydrochloric (HCl) acid under constant stirring. The acidic gas was then channelled into the vial containing the dye-loaded gellan gum. The reaction was continued until the top part of gellan gum completely turned yellow.

The reaction was recorded using a Canon camera (PowerShot G7X Mark III) and the snapshots at different timing were exported and analysed using ImageJ software. The colour of the hydrogel was analysed by splitting into RGB channels. The absolute yellow index was calculated based on the most sensitive green channel and normalized with respect to their background colour. The normalized yellow index was the absolute yellow index normalized to (0,1) with respect to the maxima.

2.12 Plasmonic catalysis for nitrogen-to-ammonia transformation

A custom quartz photoreactor was used to hold 25 mL of ultrapure water as an exterior water pool to continuously re-hydrate the hydrogel. The Ag superlattice/GG (area, 2.25 cm^2) was partially immersed in the water pool with the Ag-square superlattice exposed to the gas phase. The water pool was purged with N_2 or Ar gas for at least 10 min before the plasmonic catalysis. The NRR experiments were initiated by switching on the 100 W white LED light (400 nm – 750 nm, 277mW/cm^2) and the reaction was conducted for 1 hour. The gas flow was maintained at ~20 sccm using mass flow controller (model no. MC-100SCCM-D; Alicat Scientific Inc.) throughout the entire experiments. A 5 mL of 1 mM H_2SO_4 was used as an acid trap for the gas outlet of photoreactor to capture any ammonia gas present in the gas stream. Ammonia generated was quantified using the indophenol blue method. All plasmonic catalytic experiments were performed under constant gas flow (20 sccm) and at ambient conditions of 1 atm and 298 K. The reaction time was set at one hour per cycle to minimize any light blocking from water condensation on photoreactor setup.

2.13 Preparation of reagents for indophenol blue method

Two precursor solutions were needed in the indophenol blue method and were named as reagent A and reagent B, respectively.[41] Reagent A was prepared by dissolving phenol (0.1 M) and sodium nitroprusside dihydrate (0.2 mM) in water. Reagent B was prepared by dissolving sodium dichloroisocyanurate dihydrate (2.8 mM) and NaOH (0.13 M) in water. Both reagents were stored in the fridge before use.

2.14 Detection and quantification of ammonia in solution using indophenol blue method

A calibration curve relating absorption intensity with ammonia/ammonium concentration was first established for subsequent quantification of ammonia produced in the plasmonic catalytic NRR. Ammonium sulfate (10 mM) was dissolved in an aqueous sulfuric acid solution (1 mM). The ammonium sulfate was then diluted using serial dilution method to various concentrations between 10^{-7} and 10^{-4} M. After which, an equivalent amount of ultrapure water was added to all the ammonium sulfate solutions. Individual ammonium sulfate standard solution (2 mL) was added to a glass vial containing 1 ml of reagent A and 1 mL of reagent B. The mixture was allowed to react for 1 hour while being stirred at 500 rpm. Indophenol blue generated was identified and quantified using UV-visible absorption spectroscopy.

The ammonia present in the exterior water pool and in the acid trap after plasmonic catalytic nitrogen-to-ammonia conversion was also determined using a similar procedure. The exterior water pool solution was added to an equivalent amount of H_2SO_4 (1 mM), whereas the acid trap (1 mM H_2SO_4) was added to an equivalent amount of ultrapure water. 2 mL of individual solution was added to a glass vial containing 1mL of reagent A. 1 mL of reagent B was then added into the solution and allowed to react for 1 hour while being stirred at 500 rpm. Indophenol blue generated was identified and quantified using UV-visible absorption spectroscopy.

2.15 Detection and quantification of ammonia in gellan gum using indophenol blue method

To construct the calibration curve, ammonium chloride (20 mM) was dissolved in ultrapure water and then serial-diluted to various concentrations between 2.5×10^{-7} and 2×10^{-4} M. 2 mL of the ammonium chloride solution was then used to prepare gellan gum hydrogel. After which, the hydrogels with different concentration of ammonium chloride were dissolved in 8 mL NaOH (0.2 M) and sonicated to fully dissolve the hydrogels. The solution was centrifuged and 3 mL of the supernatant was added to an equivalent amount of ultrapure water, followed by 1 ml of reagent A and 1 mL of reagent B. The mixture was allowed to react for 1 hour while being stirred at 500 rpm. Indophenol blue generated was identified and quantified using UV-visible absorption spectroscopy.

The ammonia present in the gellan gum after plasmonic catalytic nitrogen-to-ammonia conversion was quantified using the same procedure as described above. 3 mL of the supernatant was added to an equivalent amount of ultrapure water, and the solution was added to a glass vial containing 1mL of reagent A. 1 mL of reagent B was then added into the solution and allowed to react for 1 hour while being stirred at 500 rpm. Indophenol blue generated was identified and quantified using UV-visible absorption spectroscopy.

2.16 Determination of rate of ammonia formation

The ammonia formation rate was calculated using the equation below,

$$r_{NH_3} = \frac{[NH_4^+] \times V}{t \times m_{Ag}}$$

where r_{NH_3} is the rate of ammonia formation (μmol/hr/g of Ag), $[NH_4^+]$ is the concentration of generated ammonium ion (equivalent to ammonia concentration), V is the volume of reaction solution, t is reaction duration, and m_{Ag} is the mass of Ag octahedra present in the plasmonic arrays.

The effective ammonia formation rate was calculated by subtracting the rate of ammonia formed under Ar flow from the rate of ammonia formed under N_2 flow. This is because potential nitrogen-containing species could be present to interfere with our catalytic experiment, such as (1) the possible entry of air into our flow system, (2) minor N_2 contaminants in Ar gas, and (3) nitrogen-containing species that could be present in our photoreactor. These background contributions are in fact common in photo/electrocatalytic systems, as nitrogen-containing species may be present in the feed gas, catalyst, electrolyte, ion-exchange membrane, ambient air, etc. Nevertheless, we have eliminated these inevitable background contributions by calculating the effective NH_3 formation rate. The effective ammonia formation rate notably isolates ammonia formation arising entirely from the N_2 input, thereby allowing a more representative comparison with other photocatalytic platforms. This approach is also commonly employed in the literatures to exclude potential background contribution from the reaction system.

2.17 Apparent quantum efficiency (AQE) for ammonia production at different wavelengths.

The AQE was obtained by performing N_2 reduction reaction under monochromatic light at different wavelengths (450, 500, 600, and 700 nm). The power intensity of the monochromatic light was measured using a VIS irradiance spectrometer with cosine corrector (AvaSpec-ULS2048CL-EVO, Avantes).

The calculation of AQE was based on:

$$AQE = \frac{N_{reacted}}{N_{incident}} \times 100\%$$

where $N_{reacted}$ and $N_{incident}$ can be obtained from

$$N_{reacted} = 3 \times N_A \times n_{NH_3}$$

$N_{reacted}$ is the number of reacted electrons, n_{NH_3} is the amount of ammonia produced (mol), N_A is Avogadro constant (6.022×10^{23} mol^{-1}).

$$N_{incident} = \frac{Pt}{hv} = \frac{ISt\lambda}{hc}$$

$N_{incident}$ is the number of incident photons, P is light power (W), t is illumination time (s), h is Planck constant (6.626×10^{-34} J s), v is the light frequency (Hz), I is light intensity (W cm^{-2}), S is the irradiated area (cm^2), λ is the wavelength of monochromatic light (m), and c is the speed of light in free space (3×10^8 m s^{-1}).

2.18 Finite-difference time-domain (FDTD) simulations of Ag octahedron and Ag-square superlattice

The scattering and absorption profiles of our Ag octahedron and Ag-square superlattice were confirmed by additional finite-difference time-domain (FDTD) simulations. The optical performance of the silver (Ag) octahedra are simulated by the FDTD solver from Ansys. Lumerical. The geometrical model is built based on the experiment, where Ag octahedra has a length of 452 nm standing up on the substrate (index defined as 1.4). The refractive index of Ag was taken from the default materials database of FDTD solver which was based on the CRC Handbook of Chemistry & Physics[42]. The total-field scattered-field (TFSF) source with wavelength range of 300~1000 nm was taken as the incident light source. The symmetric and anti-symmetric boundary conditions were applied in the direction perpendicular to the light irradiation. The perfectly matched layer (PML) was taken as the boundary condition along the light irradiation. The mesh size of Ag octahedra was set as 2 nm and two analysis groups of power monitors were applied to measure the absorption and scattering cross sections within the whole wavelength range.

2.19 Detection and quantification of hydrogen gas in photocatalytic NRR

A typical photoreactor setup for photocatalytic NRR was used, but modified with the gas outlet directed into a balloon to collect the evolved gas instead of connecting to an acid trap. The evolved gas was analyzed by injecting 0.8 mL of the collected gas into a gas chromatograph (SRI Multiple Gas Analyzer #5) equipped with a thermal conductivity detector (GC-TCD).

2.20 Material characterization

Scanning electron microscopy (SEM) characterizations were performed with JEOL-JSM-7600F microscope. Si wafer were cleaned using oxygen plasma (FEMTO SCIENCE, CUTE-MP/R, 100 W) for 5 min. Ag films were deposited using a thermal evaporator deposition system from Syskey Technology Corporation (Taiwan). UV-visible absorption spectroscopic measurement was conducted with a AvaSpec-ULS2048CL-EVO-UA-50 equipped with a deuterium-halogen light source (AvaLight-DH-S). SERS measurements were performed using x-y hyperspectral imaging mode of the Ramantouch microspectrometer (Nanophoton Inc, Osaka, Japan) with an excitation wavelength of 532

nm. Using a 20× (N.A. 0.45) objective lens, the effective laser power after the quartz glass was set at 0.1 mW with 10 s accumulation time. All SERS spectra were the average of at least 3 individual spectra. Contact angles were measured on a Theta Lite tensiometer equipped with a Firewire digital camera. Static contact angle was measured with a 4-μl ultrapure sessile water droplet. A total of three readings were taken at different spots on the same substrate and averaged to obtain the bulk contact angles. Diffuse reflectance measurement was conducted with an AvaSpec-ULS2048CL-EVO-UA-50 and an integrating sphere containing a halogen light source (AvaSphere-50-LS-HAL-12V). Irradiance of LED lights were measured with an AvaSpec-ULS2048CL-EVO-UA-50 and a cosine corrector (CC-VIS/NIR) with 3.9 mm diameter of active area. X-ray photoelectron spectroscopy (XPS) characterizations were measured using a Phoibos 100 spectrometer with a monochromatic Al X-ray radiation source. All XPS spectra were calibrated against high resolution C 1s peak at 284.5 eV. Photocurrent measurements were conducted with CorrTest Electrochemical Workstation CS350. A thermocouple thermometer (UNI-T UT3200) was used to measure the temperature of water pool in the reaction setup under light irradiation. The surface temperature of Ag superlattice/GG was measured with an Infrared camera (FLIR E96 24°). The video and snapshots of gellan gum were taken using a Canon camera (PowerShot G7X Mark III).

3. Results and discussion

The strategic arrangement of Ag octahedra on the hydrogel plays a vital role in generating intense electromagnetic hotspots directly at the three-phase interface (i.e., solid-liquid-gas interface) for efficient plasmon catalysis (Figure 1A). We begin by synthesizing Ag octahedra using the polyol reduction method (edge length, 452 ± 14 nm, Figure S1, S2) with poly(vinylpyrrolidone) (PVP) serving as a capping agent.[43,44] The PVP capping agent on the as-synthesized Ag octahedra is then replaced with dodecanethiol ($C_{12}SH$) via Ag-S bond formation to impart hydrophobicity (static contact angle, $\approx$130°; Figure S3) on Ag surface, a vital attribute for guiding the subsequent self-assembly process.[45,46] The successful surface modification of the Ag nanoparticles with $C_{12}SH$ is confirmed through its vibrational fingerprint in the surface-enhanced Raman spectroscopy (SERS) spectrum and the emergence of characteristic Ag-S features in the X-ray photoelectron spectroscopy (XPS) analysis (Figure S4, S5).

Next, we prepare the two-dimensional (2D) plasmonic superlattice using our previously reported liquid-liquid interfacial self-assembly approach to organize and position the $C_{12}SH$-modified Ag octahedra at the water-decane interface.[26,44] This process is governed by the minimization of free energy within the liquid-solid-liquid system. The assembled Ag octahedra are subsequently immobilized on a hydrogel surface (gellan gum; area, $\approx$2.25 cm^2, Figure 1B). Gellan gum (GG) is chosen as a model hydrogel due to its ability to stably lock the superlattice structural configuration upon solidification and to provide an aqueous reaction medium for nitrogen reduction.[47] SEM imaging of the as-prepared platform reveals that the monolayer of $C_{12}SH$-capped Ag octahedra adopt an upright orientation with a unique edge-to-edge alignment (Figure 1C, S6), leading to the formation of an ordered, square-based particle superlattice. Notably, we use this square-based plasmonic superlattice as a proof-of-concept because our previous findings indicate its ability to efficiently concentrate light at the nanoscale for generating intense and extensive plasmonic hot-strips essential for plasmonic catalysis.[26,48] Hereon, we refer to the Ag-square superlattice assembled on gellan gum as Ag superlattice/GG (or AgSL/GG) for subsequent experiments.

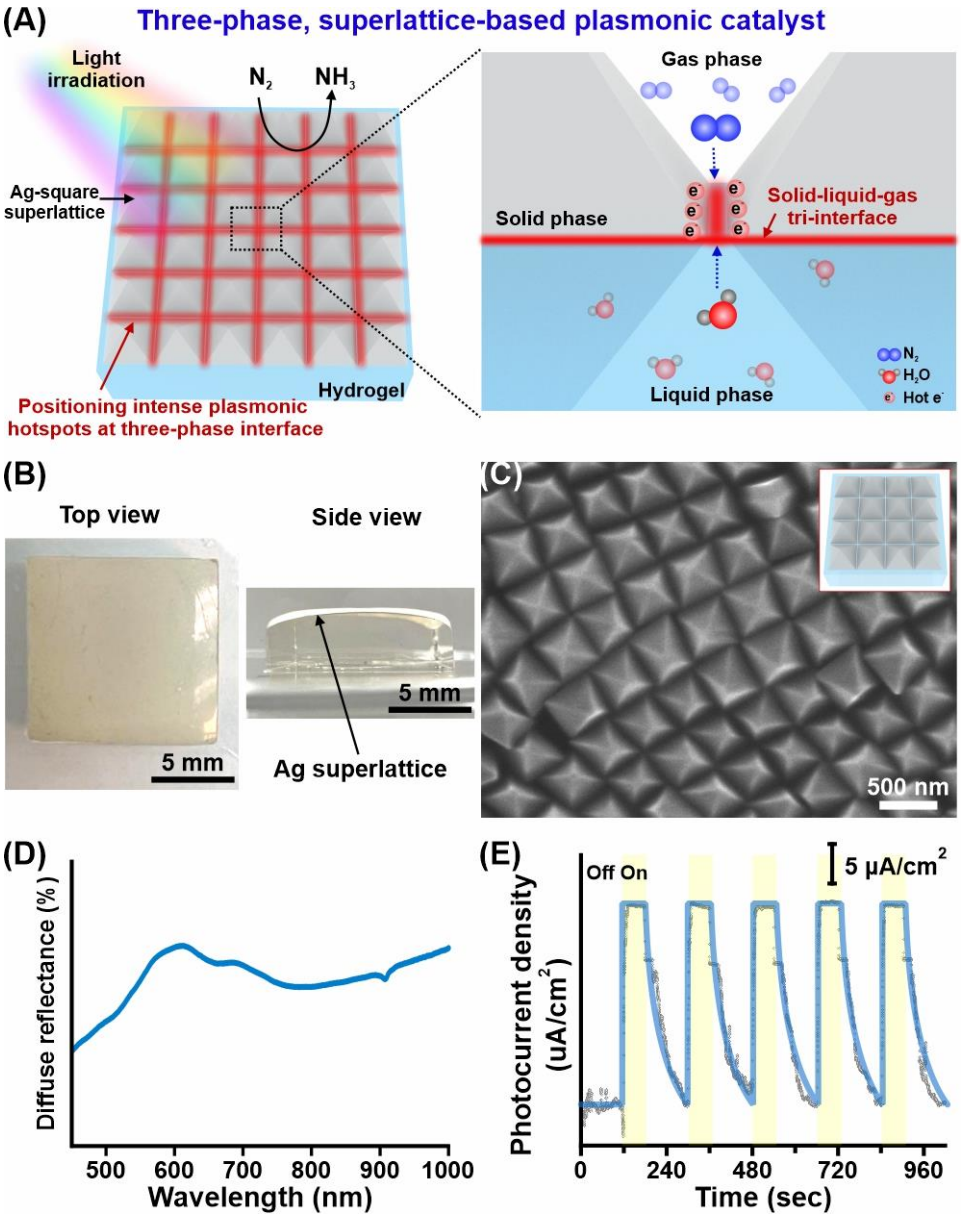

Figure 1. (A) Scheme illustrating our three-phase plasmonic catalytic design with superior light- and reactant-concentrating abilities to drive efficient nitrogen-to-ammonia transformation at ambient conditions. (B) Photograph taken from (i) top view and (ii) side view of Ag-square superlattice on hydrogel. (C) SEM image and schematic illustration (inset) of Ag-square superlattice on hydrogel. (D) Diffuse reflectance spectrum of Ag-square superlattice. (E) Photocurrent density of the Ag-square superlattice in successive on-off cycles of light irradiation.

We further investigate the optical properties of the Ag-square superlattice because they directly impact the light-to-chemical transformation. Our examination of the plasmonic superlattice includes the analysis of (i) localized surface plasmon resonances (LSPR), (ii) plasmonic field enhancement,

and the (iii) photogeneration of hot carriers as they are linked to light absorption, concentration, and utilization, respectively. Diffuse reflectance spectroscopy (DRS) measurement reveals a broad reflectance spectrum ranging from 450 – 1000 nm for the Ag-square superlattice, indicating strong light-matter interactions across the entire visible light domain. This broadband photoabsorption arises from the extensive plasmonic couplings between adjacent Ag nanoparticles (Figure 1D, S7). We also elucidate crucial insights into the Ag-square superlattice's superior ability to amplify light on the metal surfaces by quantifying the SERS enhancement factor, whereby an increase in Raman intensity could signify a corresponding enhancement in the plasmonic field.[49] In the SERS experiment, we replace the dodecanethiol molecules on the Ag surface with a self-assembled monolayer of 4-methylbenzenethiol (4-MBT) as a SERS reporter molecule. Successful replacement is verified through characteristic vibrational features at 1086 cm^{-1} (phenyl ring breathing mode and C-H in plane bending) and 1602 cm^{-1} (phenyl stretching; Figure S8A).[44] Using the SERS band at 1086 cm^{-1} as a comparison benchmark, the Ag-square superlattice exhibits a high enhancement factor of 7.4×10^4 (Figure S8B, Supporting Text 2). In contrast, a control plasmonic platform formed via the drop-casting of Ag octahedra on Si wafer (Figure S9) attains a lower SERS enhancement factor of 1.6×10^4 despite the presence of large, three-dimensional aggregates of plasmonic nanoparticles. Since both platforms employ the same Ag building block and Ag-MBT surface chemistry, this comparison evidently demonstrates the ~5-fold stronger electromagnetic field enhancement enabled by the Ag-square superlattice. The superior light-concentrating ability of the Ag-square superlattice stems from the generation of intense and large-area plasmonic hotspots that are densely distributed across the entire particle array through extensive interparticle plasmonic couplings.[44] Our finding clearly emphasizes the importance of forming highly ordered plasmonic superlattice to effectively concentrate light even with the use of the same particle building block (i.e., Ag octahedra), a feat that is otherwise challenging to achieve with conventional plasmonic platforms comprising random nanoparticle clusters.

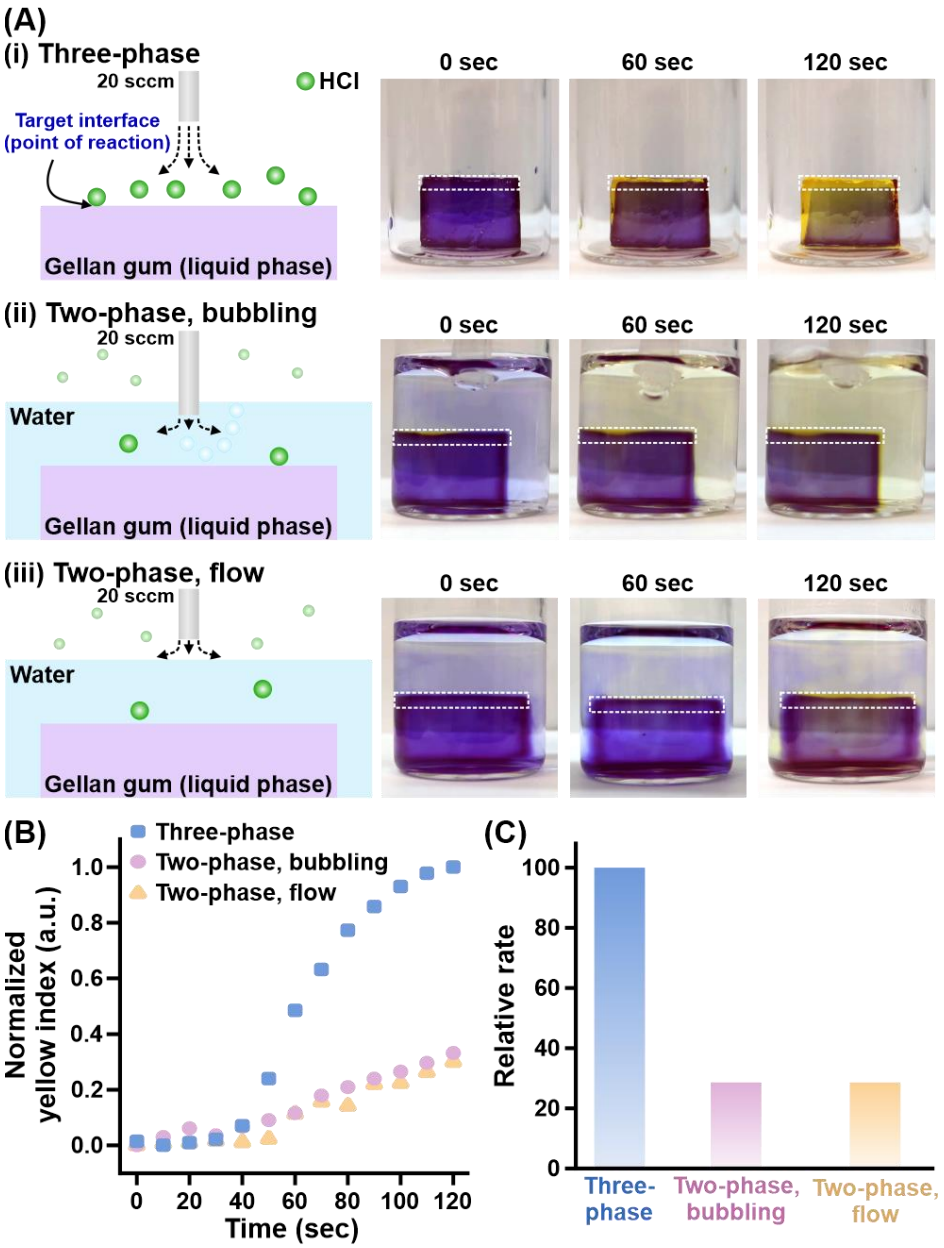

Figure 2. (A) Schemes showing different mass transfer set-ups for evaluating the accessibility of gas reactant to the target surface (white dotted box) of dye-loaded gellan gum. (i) Three-phase, (ii) two-phase, bubbling, and (iii) two-phase, flow set-ups. Bromophenol blue serves as a dye tracer to monitor chemical reactions at the target interface. (B) Time-dependent plots tracking the chemical conversion of dye tracer at the target surface region of gellan gum as observed in (A). (C) Relative rate of the flow reaction while using different mass transfer set-ups.

Moreover, transient photocurrent measurement affirms the generation of hot carriers upon plasmon decay when irradiating the Ag-square superlattice with light. It is noteworthy that we pre-

treat the Ag-square superlattice with mild acid to remove the long-chain alkylthiol on Ag surface for improving hot carrier transfer.[26] Additionally, we coat the platform with a 10 nm platinum (Pt) layer to improve its electrical conductivity but does not contribute to the photocurrent. We highlight that the Pt coating is employed only in the photocurrent evaluation and not in subsequent plasmonic catalysis (Figure S10). Upon white LED light irradiation, the acid-treated Ag-square superlattice immediately generates a stable photocurrent of ~26 μA/cm^2 which eventually diminishes when the light is switched off. This surge in photocurrent upon light irradiation supports the effective generation plasmon-induced hot carriers and their subsequent extraction from the Ag surfaces (Figure 1E). We also note that the generation of hot carriers is highly reproducible, as evident from the rapid and uniform photocurrent (<4 % deviation) recorded over five successive light on-off cycles. Such on-demand generation of energetic hot carriers upon irradiating the Ag-square superlattice with light is critical for driving photoredox reactions during nitrogen-to-ammonia transformation.

Notably, we also demonstrate the unique ability of the three-phase interfacial configuration to improve gas transfer efficiency to target reaction sites by comparing it with traditional two-phase setups. This experiment utilizes neat gellan gum (i.e., no Ag octahedra; dimension, 1.5 × 0.75 × 0.5 cm) as a demonstration due to the ease of monitoring color changes during the chemical reaction between acidic gas and a pre-loaded pH indicator in the hydrogel. The gellan gum contains basified bromophenol blue dye (pH 9) serving as a dye tracer to detect the presence and transfer of hydrochloric acid (HCl) gas at the hydrogel surface, whereby the exposure of bromophenol blue to the acidic gas induces a blue-to-yellow transition. A more intense yellow coloration thus indicates a greater extent of chemical reaction. These dye-loaded gellan gums are then placed in a gas flow cell, either directly exposed to the acidic gas environment (i.e., a three-phase design) or immersed in an exterior aqueous solution (i.e., two-phase designs) where the acidic gas (flow rate, 20 sccm) is bubbled into or flown on top of this additional liquid phase (Figure 2A). An optical camera is used to record the time-dependent color changes at the top surface of the gellan gum (i.e., side closest to gas environment), mimicking the accessibility of gas reactants to the Ag superlattice layer on the hydrogel.

Quantitative image analysis of the entire gas flow process reveals that the three-phase setup drastically promotes the transfer of gas reactant to the target reaction sites located at the top of the hydrogel. This is evidenced by a complete change from the initial blue coloration to yellow within the entire region of interest in the shortest duration of 120 s (Figure 2B). The observed yellow coloration remains consistent beyond 120 s, confirming that the chemical reaction has indeed reached completion/equilibrium. Conversely, the traditional two-phase setups exhibit a yellow coloration that is 3-fold less intense at 120 s, covering only a small <30 % of the region of interest present at the top part of the gellan gum. These comparisons highlight that the three-phase configuration enables up to ~4-fold faster reaction compared to the two-phase setups, thereby denoting a corresponding enhancement in the transfer efficiency of the gas reactant to the target reaction interface. It is also noteworthy that both the two-phase setups show similar reaction progress, regardless of whether the acidic gas is bubbled into or flown on top of the additional aqueous phase covering the hydrogel (Figure 2C and S11). The poorer mass transportation of gas reactant to the reaction interface in the traditional two-phase designs is attributed to the need for the gas reactant to first dissolve in the liquid reaction medium and be subsequently transferred to reaction sites via passive and random molecular diffusion.[50,51] This observation provides concrete evidence that the three-phase design effectively boosts the transfer efficiency and availability of gas reactants directly at the target reaction interface, notably by eliminating the need for gas reactant to pre-dissolve in a liquid medium. Overcoming this mass transport barrier in conventional two-phase reaction setups could play a vital role in facilitating efficient gas-liquid reactions, such as the nitrogen reduction reaction.

Having established its superior light- and gas-concentrating abilities, we apply the Ag superlattice/GG platform as a three-phase plasmonic catalyst to drive efficient green ammonia photosynthesis, even at ambient conditions and without the use of any sacrificial agents. The three-phase catalytic sites are located at the tri-interface formed between the plasmonic nanoparticles (solid phase), hydrogel (aqueous phase), and a N_2 or Argon (Ar) gas flow stream (gas phase; 20 sccm; Figure 3A). Prior to plasmonic catalysis, we treat the Ag superlattice/GG with aqueous acid solution to remove the long-chain alkylthiol on Ag surface, a vital step to promote both catalyst-reactant

interactions and charge transfer while preserving the structural integrity of the superlattice (Figure S12). We subsequently place the plasmonic platform in a photoreactor and partially immerse the hydrogel with an exterior water pool such that the plasmonic superlattice is directly exposed to gas phase. The hydrogel serves to continuously provide water molecules as a source of hydrogen atoms to the three-phase interface for nitrogen reduction (Figure S13), while the exterior water pool ensures that the hydrogel remains hydrated throughout the plasmonic catalysis. The plasmonic catalysis is then initiated by switching on white LED light (100 W, Figure S14) for one hour. The ammonia product is quantified using a common indophenol blue method and a concentration calibration curve obtained through UV-visible absorption spectroscopy (Figure S15, S16). After the plasmonic catalysis, we note that majority of the NH_3 generated (>86 %; Figure 3B) is present in the water pool while the remaining NH_3 is present (~14 %) in the acid trap. Interestingly, no ammonia is found in the gellan gum despite the three-phase catalysis occurring at the hydrogel's surface where Ag superlattice is situated. This observation signifies that the exterior water pool also concurrently functions to *in situ* extract the NH_3 product from the gellan gum during the catalysis. Thus, we only quantify the NH_3 present in exterior water pool and acid trap for subsequent experiments.

More importantly, our three-phase plasmonic catalyst achieves a high ammonia formation rate of ~125 μmol h^{-1} g^{-1} (Figure S17) upon light irradiation with continuous N_2 gas flow. In contrast, the control reaction setup involving Ar gas flow instead of N_2 gas shows a significantly slower ammonia formation rate of ~24 μmol h^{-1} g^{-1}, even with identical experimental conditions. By comparing the ammonia formation rate under N_2 or Ar gas flow, we determine that the three-phase plasmonic catalyst realizes an effective ammonia formation rate of ~101 μmol h^{-1} g^{-1}. This figure of merit is widely employed to effectively exclude potential background contributions from remnant dissolved N_2, air interferences, or nitrogenous chemical present in the photocatalytic setup. We also eliminate contributions from (photo)chemical effects or chemical interference from the hydrogel, as evident from the negligible ammonia present (<4 %; Figure S18) in neat gellan gum (i.e., without Ag) compared to that observed in the case of three-phase plasmonic catalysis. These results jointly

ascertain that the electromagnetically hot plasmonic superlattice is the sole catalyst, and N_2 gas is the main reactant in the ammonia photosynthesis process.

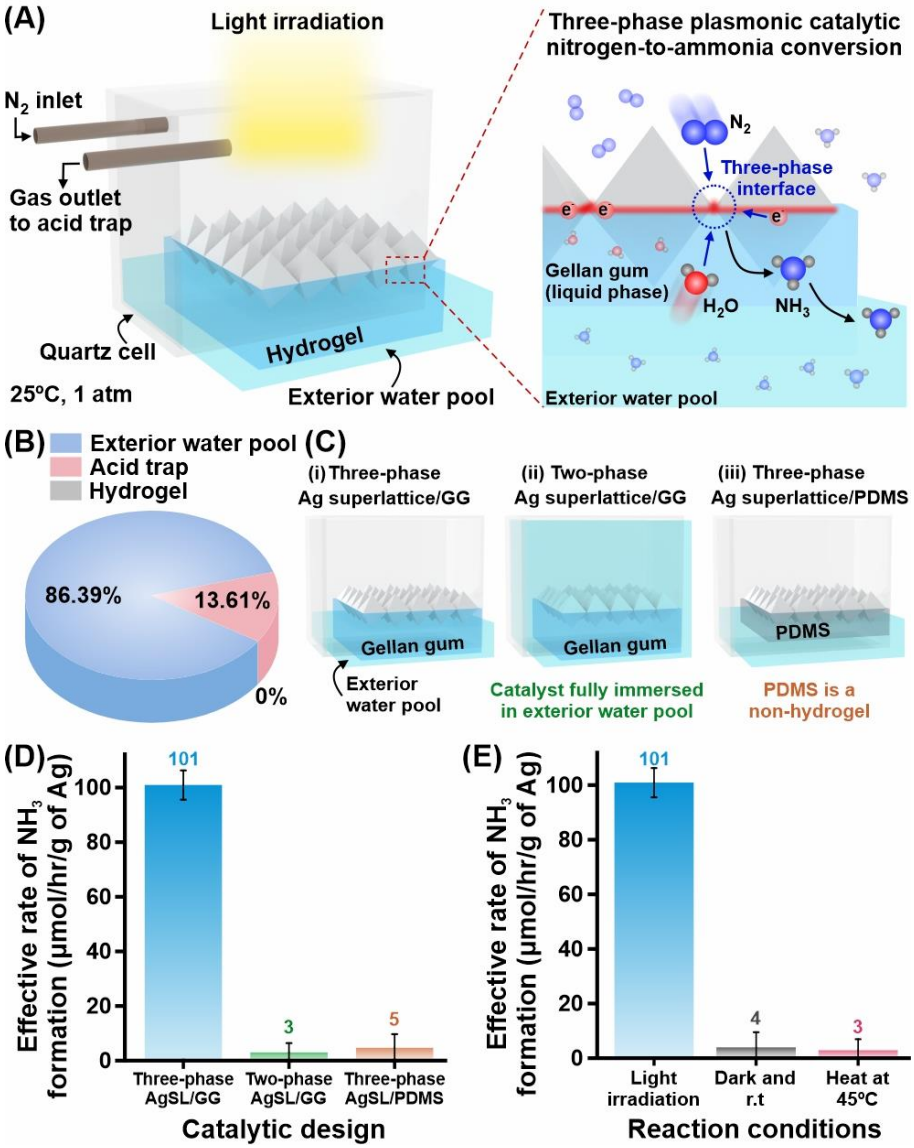

Figure 3. (A) Schematic illustration of the photoreactor set-up for the reduction of nitrogen into ammonia using the three-phase, superlattice-based plasmonic catalyst. (B) Pie chart showing the distribution of ammonia product in various parts of the photoreactor system, such as in the exterior water poor, acid trap, and gellan gum. (C) Schemes and (D) effective ammonia yield rate obtained using the Ag-square superlattice on gellan gum (Ag superlattice/GG) platform in three-phase or two-phase configurations under white light irradiation. Ag-square superlattice on PDMS (Ag superlattice/PDMS) is used as a control platform for comparison. (E) Effective ammonia yield rate of the three-phase Ag-square superlattice under different reaction conditions.

To demonstrate the crucial roles of solid-liquid-gas interfacial design and hydrogel in driving gas-liquid reactions, we conduct a comparative analysis by exploring a two-phase catalytic setup and substituting gellan gum with a non-hydrogel. These control experiments encompass (i) utilizing Ag superlattice/GG as the plasmonic catalyst fully submerged in an exterior aqueous reaction medium (i.e., two-phase setup) and (ii) employing a similar three-phase setup but replacing the gellan gum with polydimethylsiloxane (Ag superlattice/PDMS; Figure 3C). It is worth noting that the PDMS support is chosen because it maintains the structural integrity of the Ag-square superlattice, but lacks the ability to effectively absorb and transport water to the three-phase interface (i.e., non-hydrogel; Figure S19). Three key observations emerge from the systematic studies. First, our three-phase plasmonic design achieves ~34-fold higher effective ammonia formation rate compared to the two-phase Ag superlattice/GG platform (3.0 μmol h^{-1} g^{-1}; Figure 3D). This observation again affirms that the catalysis indeed occurs at the three-phase interface, underscoring the importance of converging gas (N_2) and liquid (H_2O) reactants directly on Ag catalytic surfaces for enhanced nitrogen-to-ammonia conversion. Second, the hydrogel plays a critical role in driving the nitrogen reduction reaction by facilitating the continuous supply of water reactant to the three-phase interface where the reaction occurs, as evident from the negligible ammonia formed (effective rate, ~5 μmol h^{-1} g^{-1}) when using the Ag superlattice/PDMS in a similar three-phase catalytic setup. Third, the water vapor present within the photoreactor system seemingly plays no role in facilitating the nitrogen reduction reaction, as inferred from the comparison of Ag superlattice/GG and Ag superlattice/PDMS in a three-phase configuration. These findings unequivocally emphasize that both the three-phase plasmonic interface and the hydrogel support are crucial design features enabling efficient ammonia photosynthesis.

We delve deeper into critical insights regarding the primary energy transfer mechanism in three-phase plasmonic catalysis by examining potential contributions from (i) plasmon-induced hot carrier transfer and (ii) photothermal heating. This investigation involves performing reactions (i) in the absence of light at ambient condition and (ii) without light irradiation but with the heating of the exterior water pool to 45 °C. It is important to note that the chosen reaction temperature of 45 °C aligns

with the localized surface temperature of the plasmonic superlattice (28 °C) as well as the exterior water pool's temperature (~45 °C) under white light irradiation (Figure S20). In comparison to three-phase plasmonic catalysis, both control conditions give significantly lower ammonia formation (effective rate, <4 μmol h^{-1} g^{-1}, Figure 3E) even though all experiments employ the same Ag superlattice/GG. This result clearly demonstrates that light irradiation and subsequent production of energetic hot carriers is the main driving force behind the catalytic reaction, with photothermal effect contributing minimally to the overall ammonia formation rate (<3 %).

Our comprehensive study collectively highlights the central role played by both the three-phase catalytic interface and the plasmonic superlattice in the superior performance of our unique three-phase plasmonic catalysis for ammonia photosynthesis, notably without the use of any sacrificial agents (Figure 4A). Under light irradiation, the Ag-square superlattice undergoes localized surface plasmon resonance and extensive plasmonic couplings between neighbouring particles to create intense, wide plasmonic hotspots along the particles' edges throughout the entire 2D array. The formation of such plasmonic hot-strips consequently boosts the generation of hot carriers at the solid-liquid-gas interface upon the non-radiative decay of plasmons, with the hot electrons and hot holes possessing energies well above the Ag's Fermi level (up to 2.76 eV, Figure S21). The strategic positioning of plasmonic hot-strips at the tri-interface formed between solid catalyst, hydrogel, and the gas environment proves critical in facilitating the generation of abundant hot carriers precisely at the point-of-catalysis. More importantly, the three-phase interface enables the effective convergence and enrichment of N_2 gas and water reactants at the catalytic sites, thereby promoting the interactions between originally immiscible reactants while overcoming the poor solubility of N_2 gas in most liquids. These two principal design features allow for the efficient transfer of hot electrons to N_2 gas for its subsequent transformation into ammonia product. Notably, the photogenerated holes are likely consumed by water molecules through oxidation into oxygen gas, as no other molecular agent is present in the aqueous hydrogel phase. Moreover, the potential of water oxidation at 1.23 V is close to the Fermi level of Ag, thereby enabling the effective transfer of generated hot holes to water molecules for their oxidation reactions. This observation suggests that the three-phase design also

facilitates the oxygen evolution reaction from water, possibly due to the effective removal of O_2 product into the continuous gas phase. This phenomenon prevents the nucleation of O_2 gas into nano/microbubbles which would otherwise inhibit catalytic sites and require additional energy input for subsequent reactions. By concentrating hot carriers and biphasic reactants directly at the functional three-phase interface, our unique design critically enhances the generation and utilization of hot carriers for achieving efficient ammonia photosynthesis.

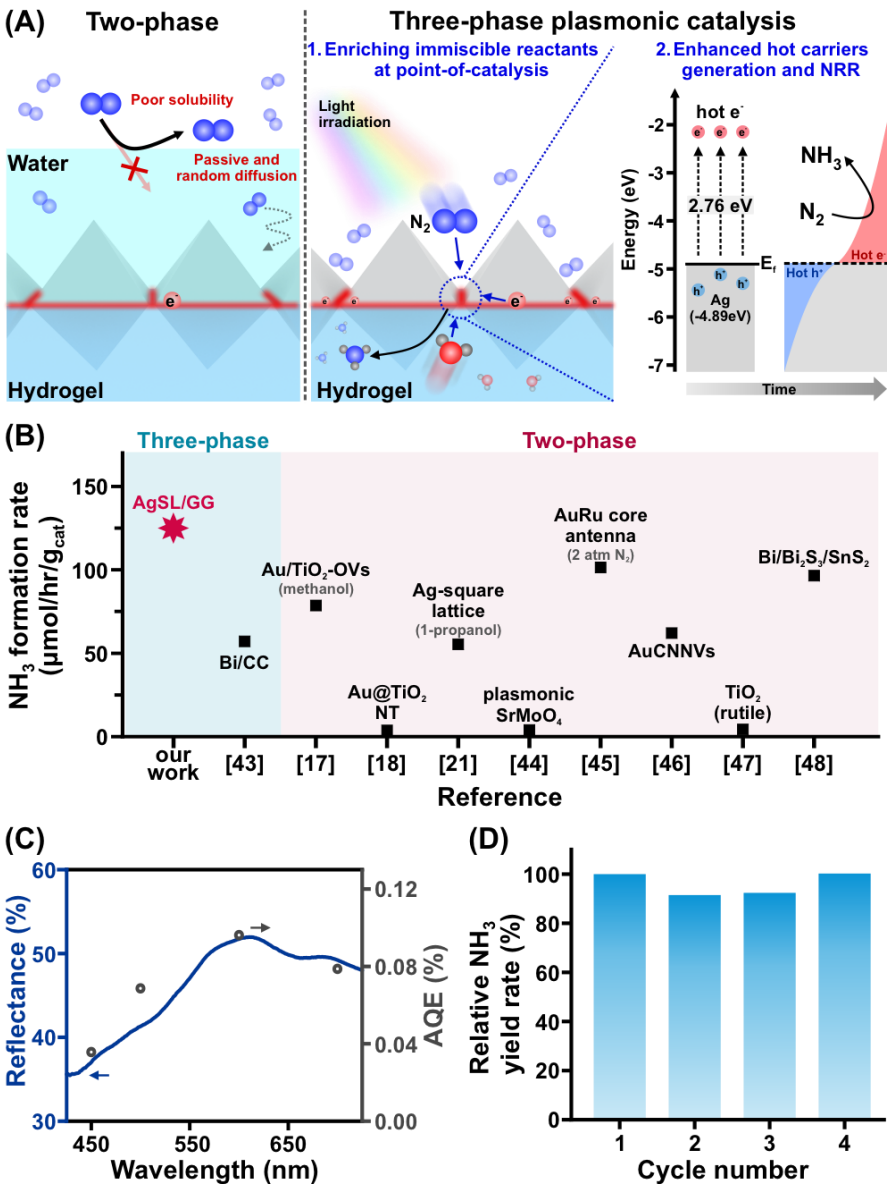

Figure 4. (A) Proposed mechanism illustrating the origin of enhanced NRR when using our three-phase plasmonic catalytic design. Traditional two-phase configuration formed using the same Ag-square superlattice is also included for comparison. (B) Comparison of ammonia yield rate obtained

through our three-phase plasmonic catalyst with other emerging plasmonic/photocatalytic designs. The hole scavengers or the elevated reaction pressure used are indicated in the parentheses. (C) Diffuse reflectance spectrum of Ag-square superlattice and the corresponding apparent quantum efficiency (AQE) under various monochromatic light irradiation. (D) Ammonia yield rate obtained using the three-phase, superlattice-based plasmonic catalysts over four repeated reaction cycles.

Interestingly, our three-phase plasmonic catalyst building on a hydrogel as the liquid phase and comprising only a single-particle-thick layer of nanocatalysts is unprecedented in both conventional plasmonic catalysis and three-phase catalysis. This unique design offers the advantage of creating abundant three-phase contact points for catalytic reaction with minimum nanocatalyst usage, thereby allowing for a more efficient utilization of light energy, catalytic materials, and reactant molecules. The superior performance of our three-phase plasmonic design is evident as it outperforms traditional two-phase catalysis by ~33-fold. Furthermore, it also showcases up to ~26-fold and ~2500-fold enhancements in ammonia formation rate and apparent quantum yield (details in next paragraph), respectively, compared to other emerging two-phase or three-phase photocatalytic platforms, even when the latter uses precious metal as co-catalysts and/or organic hole scavengers (Figure 4B, Table S1).[17,18,26,52-57] While the photogenerated electrons can also drive the hydrogen evolution reaction (Figure S22), it is evident that the three-phase plasmonic design is necessary to boost nitrogen-to-ammonia photosynthesis without needing additional co-catalysts or sacrificial agents.

We also note that the photocatalytic performance of the three-phase Ag superlattice/GG can be readily modulated by controlling the wavelength of light irradiation. Monochromatic light irradiation in the range of 450 - 700 nm (Figure S23) reveals that the trend of AQE (based on ammonia formation) closely aligns with the LSPR of the Ag-square superlattice, attaining a maximum AQE of ~0.1 % under 600 nm light irradiation (Figure 4C, Supporting Text 3). The direct correlation between catalytic performances and light irradiation wavelength clearly indicates that the enhanced nitrogen reduction reaction (NRR) indeed originates from the strong light-matter interactions of the plasmonic array. The Ag superlattice/GG ensemble can be readily reused without requiring additional treatment, as

demonstrated by the consistent ammonia yield rate (<5 % deviation) over four successive cycles (Figure 4D). Further examinations of the three-phase plasmonic catalyst's surface chemistry and morphology also highlight its excellent structural and chemical robustness against potential detrimental catalyst poisoning or degradation after prolonged usage (Figure S24, S25).

4. Conclusion

In summary, we have introduced a three-phase plasmonic catalyst with superior light-concentrating and reactant-enriching abilities to efficiently convert nitrogen gas into valuable chemical (ammonia) under light irradiation. Our strategy leverages the strategic positioning of a single-particle-thick plasmonic superlattice at the point-of-reaction to create large-area, intense plasmonic hotspots for facile reaction activation while maximizing light/catalyst utilization. The Ag superlattice/GG platform achieves a superior effective ammonia formation rate of 101 μmol h^{-1} g^{-1} even without the use of any sacrificial agent, notably surpassing conventional two-phase configuration by ~33-fold. More importantly, our unique three-phase plasmonic catalyst attains up to ~26-fold and ~2500-fold enhancements in ammonia formation rate and apparent quantum yield, respectively, compared to other emerging two-phase or three-phase photocatalytic platforms, even when the latter utilizes precious metal as co-catalysts and/or organic hole scavengers. Further mechanistic investigation underscores the importance of the three-phase plasmonic interface in concurrently enriching immiscible liquid-gas reactants and concentrating light on catalytic surfaces for enhanced plasmon-driven nitrogen fixation. By establishing an electromagnetically hot three-phase interface, our work provides valuable insights for effectively manipulating molecules and light at the nanoscale in the future design of high-performance plasmonic ensembles. These benefits will expedite our progress towards achieving efficient and truly green ammonia photosynthesis, as well as enhancing gas-liquid reactions for diverse applications, such as CO_2 valorization, toxic gas remediation, and chemical synthesis.

Declaration of Competing Interest

The authors declare that they have no known competing financial interests or personal relationships that could have appeared to influence the work reported in this paper.

Data availability

Data will be made available on request.

Acknowledgements

H.K.L. thanks the funding supports from the Singapore Ministry of Education (AcRF Tier 1 RS13/20 and RG4/21), A*STAR Singapore (MTC IRG M23M6c0098, AME YIRG A2084c0158), the National University of Singapore Center of Hydrogen Innovation (CHI-P2022-05), and the Nanyang Technological University start-up grants. The research was conducted as a part of NICES (NTU-IMRE Chemistry Lab for Eco Sustainability; REQ0275931), a joint research initiative between Nanyang Technological University (NTU) and Institute of Materials Research and Engineering (IMRE) from Agency for Science, Technology, and Research (A*STAR). S.K.B. thanks the funding support from the Leave a Nest Grant Global Challenge Award in Singapore.

Appendix A. Supporting Information

Supporting information associated with this article can be found in the online version at xx.

References

[1] L. Yuan, B.B. Bourgeois, C.C. Carlin, F.H.d. Jornada, J.A. Dionne, Sustainable chemistry with plasmonic photocatalysts, Nanophotonics 12 (2023) 2745-2762. https://doi.org/doi:10.1515/nanoph-2023-0149.

[2] V. Rosca, M. Duca, M.T. de Groot, M.T.M. Koper, Nitrogen Cycle Electrocatalysis, Chem. Rev. 109 (2009) 2209-2244. https://doi.org/10.1021/cr8003696.

[3] D.E. Canfield, A.N. Glazer, P.G. Falkowski, The Evolution and Future of Earth's Nitrogen Cycle, Science 330 (2010) 192-196. https://doi.org/doi:10.1126/science.1186120.

[4] J. John, D.-K. Lee, U. Sim, Photocatalytic and electrocatalytic approaches towards atmospheric nitrogen reduction to ammonia under ambient conditions, Nano Converg. 6 (2019) 15. https://doi.org/10.1186/s40580-019-0182-5.

[5] D. Ye, S.C.E. Tsang, Prospects and challenges of green ammonia synthesis, Nat. Synth. 2 (2023) 612-623. https://doi.org/10.1038/s44160-023-00321-7.

[6] U. Aslam, V.G. Rao, S. Chavez, S. Linic, Catalytic conversion of solar to chemical energy on plasmonic metal nanostructures, Nat. Catal. 1 (2018) 656-665. https://doi.org/10.1038/s41929-018-0138-x.

[7] M. Dhiman, Plasmonic nanocatalysis for solar energy harvesting and sustainable chemistry, J. Mater. Chem. A . 8 (2020) 10074-10095. https://doi.org/10.1039/D0TA03114C.

[8] Z. Zhang, C. Zhang, H. Zheng, H. Xu, Plasmon-Driven Catalysis on Molecules and Nanomaterials, Acc. Chem. Res. 52 (2019) 2506-2515. https://doi.org/10.1021/acs.accounts.9b00224.

[9] M. Sui, S. Kunwar, P. Pandey, J. Lee, Strongly confined localized surface plasmon resonance (LSPR) bands of Pt, AgPt, AgAuPt nanoparticles, Sci. Rep. 9 (2019) 16582. https://doi.org/10.1038/s41598-019-53292-1.

[10] A.J. Bagnall, S. Ganguli, A. Sekretareva, Hot or Not? Reassessing Mechanisms of Photocurrent Generation in Plasmon-Enhanced Electrocatalysis, Angew. Chem. Int. Ed. n/a e202314352. https://doi.org/https://doi.org/10.1002/anie.202314352.

[11] N.-N. Vu, S. Kaliaguine, T.-O. Do, Plasmonic Photocatalysts for Sunlight-Driven Reduction of CO2: Details, Developments, and Perspectives, ChemSusChem 13 (2020) 3967-3991. https://doi.org/https://doi.org/10.1002/cssc.202000905.

[12] S.L. Foster, S.I.P. Bakovic, R.D. Duda, S. Maheshwari, R.D. Milton, S.D. Minteer, M.J. Janik, J.N. Renner, L.F. Greenlee, Catalysts for nitrogen reduction to ammonia, Nat. Catal. 1 (2018) 490-500. https://doi.org/10.1038/s41929-018-0092-7.

[13] C. Flavell-While, Fritz Haber and Carl Bosch – Feed the World, https://www.thechemicalengineer.com/features/cewctw-fritz-haber-and-carl-bosch-feed-the-world/, 2010.

[14] J.W. Erisman, M.A. Sutton, J. Galloway, Z. Klimont, W. Winiwarter, How a century of ammonia synthesis changed the world, Nat. Geosci. 1 (2008) 636-639. https://doi.org/10.1038/ngeo325.

[15] Green ammonia synthesis, Nat. Synth. 2 (2023) 581-582. https://doi.org/10.1038/s44160-023-00362-y.

[16] X. Zhang, Y.L. Chen, R.-S. Liu, D.P. Tsai, Plasmonic photocatalysis, Rep. Prog. Phys. 76 (2013) 046401. https://doi.org/10.1088/0034-4885/76/4/046401.

[17] J. Yang, Y. Guo, R. Jiang, F. Qin, H. Zhang, W. Lu, J. Wang, J.C. Yu, High-Efficiency "Working-in-Tandem" Nitrogen Photofixation Achieved by Assembling Plasmonic Gold Nanocrystals on Ultrathin Titania Nanosheets, J. Am. Chem. Soc. 140 (2018) 8497-8508. https://doi.org/10.1021/jacs.8b03537.

[18] S. Chang, X. Xu, Au nanocrystals decorated TiO2 nanotubes for photocatalytic nitrogen fixation into ammonia, Inorganic Chemistry Frontiers 7 (2020) 620-624. https://doi.org/10.1039/C9QI01287G.

[19] H. Li, J. Zhang, X. Deng, Y. Wang, G. Meng, R. Liu, J. Huang, M. Tu, C. Xu, Y. Peng, B. Wang, Y. Hou, Structure and Defect Engineering Synergistically Boost High Solar-to-Chemical Conversion Efficiency of Cerium oxide/Au Hollow Nanomushrooms for Nitrogen Photofixation, Angew. Chem. Int. Ed. n/a e202316384. https://doi.org/https://doi.org/10.1002/anie.202316384.

[20] T. Hou, L. Chen, Y. Xin, W. Zhu, C. Zhang, W. Zhang, S. Liang, L. Wang, Porous CuFe for Plasmon-Assisted N2 Photofixation, ACS Energy Letters 5 (2020) 2444-2451. https://doi.org/10.1021/acsenergylett.0c00959.

[21] H. Yin, J. Hu, C. Fang, Y. Wang, L. Ma, N. Zhang, S. Zhang, R. Jiang, J. Wang, Highly efficient electrocatalytic nitrogen fixation enabled by the bridging effect of Ru in plasmonic nanoparticles, Nano Research 16 (2023) 360-370. https://doi.org/10.1007/s12274-022-4842-0.

[22] M. Nazemi, M.A. El-Sayed, Plasmon-enhanced photo(electro)chemical nitrogen fixation under ambient conditions using visible light responsive hybrid hollow Au-Ag2O nanocages, Nano Energy 63 (2019) 103886. https://doi.org/https://doi.org/10.1016/j.nanoen.2019.103886.

[23] X. Cui, Y. Chen, M. Zhang, Y.W. Harn, J. Qi, L. Gao, Z.L. Wang, J. Huang, Y. Yang, Z. Lin, Tailoring carrier dynamics in perovskite solar cells via precise dimension and architecture control and interfacial positioning of plasmonic nanoparticles, Energy & Environmental Science 13 (2020) 1743-1752. https://doi.org/10.1039/C9EE03937F.

[24] X. Liu, J. Iocozzia, Y. Wang, X. Cui, Y. Chen, S. Zhao, Z. Li, Z. Lin, Noble metal–metal oxide nanohybrids with tailored nanostructures for efficient solar energy conversion, photocatalysis and environmental remediation, Energy & Environmental Science 10 (2017) 402-434. https://doi.org/10.1039/C6EE02265K.

[25] T. Oshikiri, K. Ueno, H. Misawa, Plasmon-Induced Ammonia Synthesis through Nitrogen Photofixation with Visible Light Irradiation, Angew. Chem. Int. Ed. 53 (2014) 9802-9805. https://doi.org/https://doi.org/10.1002/anie.201404748.

[26] S.K. Boong, C. Chong, J.-K. Lee, Z.Z. Ang, H. Li, H.K. Lee, Superlattice-based Plasmonic Catalysis: Concentrating Light at the Nanoscale to Drive Efficient Nitrogen-to-Ammonia Fixation at Ambient Conditions, Angew. Chem. Int. Ed. 62 (2023) e202216562. https://doi.org/https://doi.org/10.1002/anie.202216562.

[27] R. Battino, T.R. Rettich, T. Tominaga, The Solubility of Nitrogen and Air in Liquids, Journal of Physical and Chemical Reference Data 13 (1984) 563-600. https://doi.org/10.1063/1.555713.

[28] R.T. Ferrell, D.M. Himmelblau, Diffusion coefficients of nitrogen and oxygen in water, J. Chem. Eng. Data. 12 (1967) 111-115. https://doi.org/10.1021/je60032a036.

[29] M. Ali, F. Zhou, K. Chen, C. Kotzur, C. Xiao, L. Bourgeois, X. Zhang, D.R. MacFarlane, Nanostructured photoelectrochemical solar cell for nitrogen reduction using plasmon-enhanced black silicon, Nat. Commun. 7 (2016) 11335. https://doi.org/10.1038/ncomms11335.

[30] S. Mansingh, K.K. Das, S. Sultana, K. Parida, Recent advances in wireless photofixation of dinitrogen to ammonia under the ambient condition: A review, J. Photochem. Photobiol. C: Photochem. Rev. 47 (2021) 100402. https://doi.org/https://doi.org/10.1016/j.jphotochemrev.2021.100402.

[31] J. Xu, X. Xiao, Z. Zhang, Y. Wu, D.T. Boyle, H.K. Lee, W. Huang, Y. Li, H. Wang, J. Li, Y. Zhu, B. Chen, W. Mitch, Y. Cui, Designing a Nanoscale Three-phase Electrochemical Pathway to Promote Pt-catalyzed Formaldehyde Oxidation, Nano Letters 20 (2020) 8719-8724. https://doi.org/10.1021/acs.nanolett.0c03560.

[32] R. Shi, L. Shang, T. Zhang, Three Phase Interface Engineering for Advanced Catalytic Applications, ACS Appl. Energy Mater. 4 (2021) 1045-1052. https://doi.org/10.1021/acsaem.0c02989.

[33] H. Jiang, R. Luo, Y. Li, W. Chen, Recent advances in solid–liquid–gas three-phase interfaces in electrocatalysis for energy conversion and storage, EcoMat 4 (2022) e12199. https://doi.org/https://doi.org/10.1002/eom2.12199.

[34] H. Yang, C. Nan, N. Gao, W. Zhou, F. Gao, D. Dong, D. Dou, Y. Liu, Z. Liang, D. Yang, Three-phase interface of SnO2 nanoparticles loaded on hydrophobic MoS2 enhance photoelectrochemical N2 reduction, Electrochim. Acta 430 (2022) 141086. https://doi.org/https://doi.org/10.1016/j.electacta.2022.141086.

[35] J. Zhang, B. Zhao, W. Liang, G. Zhou, Z. Liang, Y. Wang, J. Qu, Y. Sun, L. Jiang, Three-Phase Electrolysis by Gold Nanoparticle on Hydrophobic Interface for Enhanced Electrochemical Nitrogen Reduction Reaction, Adv. Sci. 7 (2020) 2002630. https://doi.org/https://doi.org/10.1002/advs.202002630.

[36] A. Li, Q. Cao, G. Zhou, B.V.K.J. Schmidt, W. Zhu, X. Yuan, H. Huo, J. Gong, M. Antonietti, Three-Phase Photocatalysis for the Enhanced Selectivity and Activity of CO2 Reduction on a

Hydrophobic Surface, Angew. Chem. Int. Ed. 58 (2019) 14549-14555. https://doi.org/https://doi.org/10.1002/anie.201908058.

[37] J. Li, G. Chen, Y. Zhu, Z. Liang, A. Pei, C.-L. Wu, H. Wang, H.R. Lee, K. Liu, S. Chu, Y. Cui, Efficient electrocatalytic CO2 reduction on a three-phase interface, Nat. Catal. 1 (2018) 592-600. https://doi.org/10.1038/s41929-018-0108-3.

[38] Z. Xing, L. Hu, D.S. Ripatti, X. Hu, X. Feng, Enhancing carbon dioxide gas-diffusion electrolysis by creating a hydrophobic catalyst microenvironment, Nat. Commun. 12 (2021) 136. https://doi.org/10.1038/s41467-020-20397-5.

[39] J. Li, Y. Zhu, W. Chen, Z. Lu, J. Xu, A. Pei, Y. Peng, X. Zheng, Z. Zhang, S. Chu, Y. Cui, Breathing-Mimicking Electrocatalysis for Oxygen Evolution and Reduction, Joule 3 (2019) 557-569. https://doi.org/https://doi.org/10.1016/j.joule.2018.11.015.

[40] Y.H. Lee, W. Shi, H.K. Lee, R. Jiang, I.Y. Phang, Y. Cui, L. Isa, Y. Yang, J. Wang, S. Li, X.Y. Ling, Nanoscale surface chemistry directs the tunable assembly of silver octahedra into three two-dimensional plasmonic superlattices, Nat. Commun. 6 (2015) 6990. https://doi.org/10.1038/ncomms7990.

[41] A. Tsuneto, A. Kudo, T. Sakata, Lithium-mediated electrochemical reduction of high pressure N2 to NH3, J. Electroanal. Chem. 367 (1994) 183-188. https://doi.org/https://doi.org/10.1016/0022-0728(93)03025-K.

[42] H.J. Hagemann, W. Gudat, C. Kunz, Optical constants from the far infrared to the x-ray region: Mg, Al, Cu, Ag, Au, Bi, C, and Al2O3, J. Opt. Soc. Am. 65 (1975) 742-744. https://doi.org/10.1364/JOSA.65.000742.

[43] A. Tao, P. Sinsermsuksakul, P. Yang, Polyhedral Silver Nanocrystals with Distinct Scattering Signatures, Angew. Chem. Int. Ed. 45 (2006) 4597-4601. https://doi.org/https://doi.org/10.1002/anie.200601277.

[44] Y.H. Lee, W. Shi, H.K. Lee, R. Jiang, I.Y. Phang, Y. Cui, L. Isa, Y. Yang, J. Wang, S. Li, X.Y. Ling, Nanoscale surface chemistry directs the tunable assembly of silver octahedra into three two-dimensional plasmonic superlattices, Nat. Commun. 6 (2015) https://doi.org/10.1038/ncomms7990.

[45] Q. Yao, Z. Wu, Z. Liu, Y. Lin, X. Yuan, J. Xie, Molecular reactivity of thiolate-protected noble metal nanoclusters: synthesis, self-assembly, and applications, Chem. Sci. 12 (2021) 99-127. https://doi.org/10.1039/D0SC04620E.

[46] A. Castelli, J. de Graaf, S. Marras, R. Brescia, L. Goldoni, L. Manna, M.P. Arciniegas, Understanding and tailoring ligand interactions in the self-assembly of branched colloidal nanocrystals into planar superlattices, Nat. Commun. 9 (2018) 1141. https://doi.org/10.1038/s41467-018-03550-z.

[47] Z. Luo, X. Mu, Y.S. Zhang, Chapter 3 - Biomaterials for bioprinting, in: M. Conti, M. Marino (Eds.), Bioprinting, Academic Press, 2022, pp. 51-86.

[48] D. Liu, C. Xue, Plasmonic Coupling Architectures for Enhanced Photocatalysis, Advanced Materials 33 (2021) 2005738. https://doi.org/https://doi-org.remotexs.ntu.edu.sg/10.1002/adma.202005738.

[49] H.K. Lee, Y.H. Lee, C.S.L. Koh, G.C. Phan-Quang, X. Han, C.L. Lay, H.Y.F. Sim, Y.-C. Kao, Q. An, X.Y. Ling, Designing surface-enhanced Raman scattering (SERS) platforms beyond hotspot engineering: emerging opportunities in analyte manipulations and hybrid materials, Chem. Soc. Rev. 48 (2019) 731-756. https://doi.org/10.1039/C7CS00786H.

[50] Y. Lanoiselée, N. Moutal, D.S. Grebenkov, Diffusion-limited reactions in dynamic heterogeneous media, Nat. Commun. 9 (2018) 4398. https://doi.org/10.1038/s41467-018-06610-6.

[51] M.E. Davis, Robert J. Davis., Effects of Transport Limitations on Rates of Solid-catalyzed Reactions 6.1 I Introduction, in: Fundamentals of chemical reaction engineering, McGraw-Hill Higher Education, New York, 2003.

[52] Y. Li, J. Liu, Z. Sun, R. Li, L. Guo, X. Zhang, Y. Wang, Y. Wang, Z. Yu, C. Fan, Enhanced photocatalytic ammonia synthesis over a Bi/carbon cloth float: triphase reaction system-assisted N2 supply and photothermal co-activation, Green Chem. 24 (2022) 9253-9262. https://doi.org/10.1039/D2GC02683J.

[53] Q. Li, Z. Zhao, X. Bai, X. Tong, S. Yue, J. Luo, X. Yu, Z. Wang, Z. Wang, P. Li, Y. Liang, Z. Wang, Tunable and stable localized surface plasmon resonance in SrMoO4 for enhanced visible light

driven nitrogen reduction, Chinese J. Catal. 42 (2021) 1763-1771. https://doi.org/https://doi.org/10.1016/S1872-2067(21)63799-3.

[54] C. Hu, X. Chen, J. Jin, Y. Han, S. Chen, H. Ju, J. Cai, Y. Qiu, C. Gao, C. Wang, Z. Qi, R. Long, L. Song, Z. Liu, Y. Xiong, Surface Plasmon Enabling Nitrogen Fixation in Pure Water through a Dissociative Mechanism under Mild Conditions, J. Am. Chem. Soc. 141 (2019) 7807-7814. https://doi.org/10.1021/jacs.9b01375.

[55] S. Wu, Z. Chen, K. Liu, W. Yue, L. Wang, J. Zhang, Chemisorption-Induced and Plasmon-Promoted Photofixation of Nitrogen on Gold-Loaded Carbon Nitride Nanosheets, ChemSusChem 13 (2020) 3455-3461. https://doi.org/https://doi.org/10.1002/cssc.202000818.

[56] G.N. Schrauzer, T.D. Guth, Photolysis of Water and Photoreduction of Nitrogen on Titanium Dioxide, J. Am. Chem. Soc. 99 (1977) 7189-7193. https://doi.org/10.1021/ja00464a015.

[57] M. Lan, X. Dong, N. Zheng, X. Zhang, Y. Wang, X. Zhang, In-situ construction of novel sulfur-vacancy-rich Bi/Bi2S3/SnS2 Z-scheme heterostructure photocatalysts for efficient Cr(VI) reduction and nitrogen fixation, J. Mater. Sci. Technol. 167 (2023) 237-247. https://doi.org/https://doi.org/10.1016/j.jmst.2023.05.037.